

Melting dynamics and mixing layer growth near the ice-ocean interface

Sofía Allende¹†, Louis-Alexandre Couston², Simon Thalabard³, and Benjamin Favier¹

¹Aix Marseille Univ, CNRS, Centrale Med, IRPHE, Marseille, France.

²Université Claude Bernard Lyon 1, ENS de Lyon, CNRS, LPENSL, UMR5672, Lyon, France.

³Université Côte d'Azur, CNRS, Institut de Physique de Nice, Nice, France.

(Received xx; revised xx; accepted xx)

Ice melting into saline water plays a fundamental role in the dynamics near the ice-ocean interface in polar oceans. The physics of ice melting involves a non-trivial interplay between thermodynamics at the interface, hydrodynamic transport in the bulk and the properties of the ambient ocean. The key control parameters are the density ratio R_ρ proportional to the ambient ocean salinity and the Lewis number $Le = \kappa_T/\kappa_S$, which compares the thermal and salt diffusivities. Increasing the salinity is known to slow down melting, with the melt rate transitioning from subdiffusive to diffusive as R_ρ increases. Here, we assess the role of turbulence in this transition, using highly-resolved numerical simulations of the two-dimensional Boussinesq equations with a slowly melting upper boundary. We analyse the non-stationary growth of the temperature and meltwater mixing layers, varying the Lewis number and the density ratio. While meltwater is continuously entrained by convection inside the bulk, we identify a transition from convection to diffusion close to the interface. This transition is reflected by the formation of an interfacial boundary layer that regulates the flux of meltwater pouring into the turbulent bulk for $R_\rho \gtrsim 10$. Using mixing-layer diagnostics based on meltwater-concentration thresholds, we observe that the turbulent layer grows super-diffusively $\propto t^{1.33}$, while the interfacial boundary layer expands diffusively $\propto t^{0.5}$ but with a non-universal prefactor. These results indicate that double-diffusive effects are here confined to the interface, and highlight potential limitations of diagnostics based on fixed concentration thresholds in oceanographic applications.

1. Introduction

The melting of ice into salty water is a fundamental process that occurs in various natural environments, controlling the fate of polar ice shelves, sea ice, and glacial meltwater plumes (Hewitt 2020; Du *et al.* 2024; Rosevear *et al.* 2025). Its understanding is critical for predicting sea level rise and climate feedback mechanisms, as melting affects both local stratification and the transport of freshwater into the ocean (Jenkins 1999). Recent studies have emphasised the sensitivity of melting rates to thermodynamics at the interface (Keitzl *et al.* 2016), examined fluid instabilities caused by basal diffusion (Berhanu *et al.* 2021; Cohen *et al.* 2020), explored the role of turbulent mixing in influencing the properties of

† Email address for correspondence: sofia.allende@univ-amu.fr

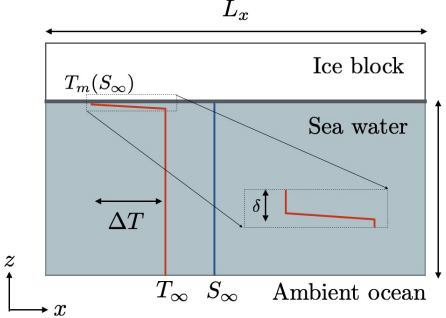


Figure 1: Initial configuration

Heat capacity of seawater	C_p	$3974 \text{ J K}^{-1} \text{ kg}^{-1}$
Latent heat	L_f	$3.35 \times 10^5 \text{ J kg}^{-1}$
Freezing slope	λ_1	$-5.73 \times 10^{-2} \text{ K} (\text{g/kg})^{-1}$
Thermal expansion	β_T	$3.87 \times 10^{-5} \text{ K}^{-1}$
Haline contraction	β_S	$7.86 \times 10^{-4} (\text{g/kg})^{-1}$
Temperature jump	ΔT	2 K
Freezing point of pure water	$T_{f,0}$	273.15 K
Kinematic viscosity	ν	$1.8 \times 10^{-6} \text{ m}^2 \text{ s}^{-1}$
Thermal diffusivity	κ_T	$1.8 \times 10^{-6} \text{ m}^2 \text{ s}^{-1}$
Gravitational acceleration	g	9.8 m s^{-2}
Depth	L_z	6.28 m
Horizontal extent	L_x	6.28 m

Table 1: Physical parameters

near-ice water (Couston 2024), and examined the asymmetries between melting and freezing within convective systems (Yang *et al.* 2025).

The recent numerical studies by Xue *et al.* (2024) and Guo & Yang (2025), employing phase-field methods, suggest that in the absence of external flow, the interface dynamics is controlled by the density ratio R_ρ —a non-dimensional number quantifying the far-field (ambient water) salinity rigorously defined in Eq. (2.5). Over relatively fresh ambient water (small R_ρ), mixing is dominated by thermal convection, and ice melts at a nearly constant rate, following a sub-diffusive scaling $\propto t^{-0.2}$. Over relatively salty ambient water (large R_ρ), the system instead develops a strongly stratified, diffusion-dominated regime, with the melt rate exhibiting a diffusive scaling $\propto t^{-0.5}$.

Here, we build on these investigations to revisit the turbulence generated by a block of freshwater ice immersed in initially quiescent, warm, salty ocean water. Our study focuses on the early-time growth of mixing layers (*i.e.*, while unaffected by the bottom boundary) and their connection to the melt rate at the ice–ocean interface. We use high-resolution numerical simulations of a vertically bounded and horizontally periodic domain, and investigate how the Lewis number (the ratio of thermal to saline diffusivity) and the density ratio impact the dynamics. In our configuration, a convective mixing layer develops regardless of the parameters, which grows super-diffusively and self-similarly in time—unaffected by the melting. Over sufficiently salty environments, we recover the formation of a fresh boundary layer which regulates the amount of meltwater poured into the bulk, with ratio between the diffusive and the convective fluxes growing linearly with the density ratio. While the boundary layer produces the diffusive rate of melting, it does not suppress the bulk turbulence, nor does it significantly modify its statistics.

The paper is organized as follows: §2 describes the physical and numerical setup, §3 presents the main results, contrasting interface and bulk dynamics and discussing mixing length definitions. Finally in §4, we share some concluding remarks.

2. Numerical set-up

We consider the flow illustrated in Fig. 1, which is initially quiescent. The domain is two-dimensional (2D), with horizontal extent L_x and depth $L_z = L_x$. The initial salinity S is uniform and equal to the far-field value S_∞ , while the temperature T has a step-profile characterized by a temperature jump $\Delta T = T_\infty - T_m(S_\infty)$. This represents the difference between the far-field temperature T_∞ and the melting temperature $T_m(S_\infty) = T_{f,0} + \lambda_1 S_\infty$.

We later work with non-dimensional variables for temperature and salinity, defined as

$$\theta = \frac{T - T_\infty}{\Delta T} \quad \text{and} \quad \sigma = \frac{S - S_\infty}{\Delta S} \quad (2.1)$$

where $\Delta T := T_\infty - T_m(S_\infty)$, $\Delta S := \frac{\beta_T}{\beta_S} \Delta T$.

Here, ΔS is the salinity variation required to compensate the density change caused by ΔT , according to the linearized equation of state $\rho = \rho_0 [1 - \beta_T T + \beta_S S]$, which we adopt here for simplicity. We model the fluid dynamics with the two-dimensional incompressible Navier-Stokes equations under the Boussinesq approximation.

Defining the horizontal length L_x , the velocity $U_0 := \sqrt{2g\beta_T \Delta T L_x}$, and the time $t_0 = L_x/U_0$, as characteristic scales, the dynamics take the dimensionless form

$$\begin{aligned} \partial_t \mathbf{u} + (\mathbf{u} \cdot \nabla) \mathbf{u} + \nabla p &= Re^{-1} \Delta \mathbf{u} + \mathbf{e}_z \frac{\theta - \sigma}{2}, & \nabla \cdot \mathbf{u} &= 0, \\ \partial_t \theta + (\mathbf{u} \cdot \nabla) \theta &= Re^{-1} Pr^{-1} \Delta \theta, \\ \partial_t \sigma + (\mathbf{u} \cdot \nabla) \sigma &= Re^{-1} Pr^{-1} Le^{-1} \Delta \sigma, \end{aligned} \quad (2.2)$$

with non-dimensional parameters

$$Re = \frac{U_0 L_x}{\nu} \text{ (Reynolds)}, \quad Pr = \frac{\nu}{\kappa_T} \text{ (Prandtl)} \quad \text{and} \quad Le = \frac{\kappa_T}{\kappa_S} \text{ (Lewis)}. \quad (2.3)$$

The Prandtl and the Lewis numbers respectively represent the ratio of viscosity to thermal diffusivity and thermal to salt diffusivity.

The boundary conditions represent a (no-slip) melting ice–ocean interface at the top coupled to a far-field quiescent state at the bottom, similar to (Couston 2024). At the top boundary, the temperature θ is set equal to the local freezing temperature, which depends linearly on salinity through the slope γ_1 . This condition is supplemented by a balance between heat and haline fluxes, which determine the melt rate following the widely adopted Stefan condition (Middleton *et al.* 2021; Vreugdenhil & Taylor 2019; Gayen *et al.* 2016). The conditions read in dimensionless form

$$\begin{cases} z = 0 & (\text{melting}) : \theta = -1 - \gamma_1 \sigma \quad \text{and} \quad \left. \frac{\partial_z \sigma}{(\sigma + R_\rho)} \right|_{z=0} = Le S_t \partial_z \theta \Big|_{z=0} \\ z = -1 & (\text{far field}) : \theta = 0 \quad \text{and} \quad \sigma = 0, \end{cases} \quad (2.4)$$

with

$$R_\rho = \frac{S_\infty}{\Delta S} \text{ (Density ratio)}, \quad \gamma_1 = -\lambda_1 \frac{\beta_T}{\beta_S} \text{ (freezing coupling)}, \quad S_t = \frac{C_p}{L_f} \Delta T \text{ (Stefan)}. \quad (2.5)$$

The density ratio R_ρ characterises the far-field salinity by balancing its stabilising effect to the destabilising thermal jump; the parameter γ_1 represents a freezing coefficient coupling temperature and salt at the melting interface; the Stefan number S_t characterises the relative importance of specific and latent heat, based on the initial temperature jump at the interface. These boundary conditions are approximations that hold true only when the melting rate is slow. Essentially, they substitute the mass flux resulting from the phase change with a diffusive flux, introducing a Lewis dependence in Eq. (2.4). This approach serves as an alternative to directly solving the Stefan problem, which, strictly speaking, requires explicit treatment of a moving interface—see, *e.g.*, (Huppert 1990; Wettlaufer 2001). While phase-field methods can be employed to this end, they prove computationally expensive for small melting rates,

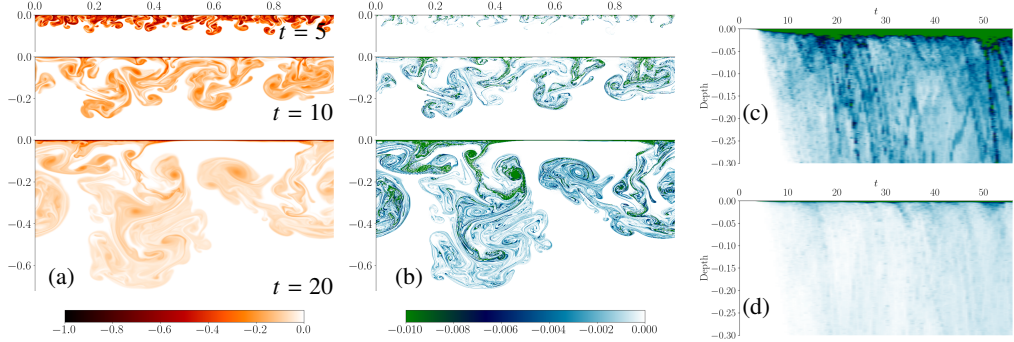


Figure 2: Typical evolution of the temperature (a) and salinity fields (b) for a simulation with $Le = 100$ and $R_\rho = 406$. Panel (c) shows the temporal evolution of the horizontally-averaged salinity profile for $R_\rho = 406$. Panel (d) shows the results for $R_\rho = 1$.

which produce a large time-scale separation between the dynamics of phase change and that of the fluid (Favier *et al.* 2019; Gastine & Favier 2025).

Our numerical setup employs direct numerical simulations using the finite-volume code Oceananigans (Ramadhan *et al.* 2020). The computational domain is discretised on a grid of 8192^2 collocation points, uniform in the horizontal direction and refined vertically near the top interface. Since Oceananigans operates with dimensional variables, all governing parameters are prescribed in physical units, for consistency with realistic seawater properties (Couston 2024; Allende *et al.* 2024). They are summarised in Table 1. The free-fall velocity and time units are $U_0 \approx 0.098 \text{ m/s}$ and $t_0 \approx 64 \text{ s}$, respectively.

In all the simulations, we set $\Delta T = 2 \text{ K}$. To explicitly satisfy the boundary conditions (2.4), we regularise the initial temperature jump by introducing a smooth temperature profile controlled by the (small) parameter $\delta \ll L_x$ —see Fig. 1. The parameter δ sets the initial gradient $\propto \Delta T/\delta$, and offsets it down from the upper boundary, at a depth $\propto \delta$. This smoothing ensures that the temperature gradient vanishes at the top boundary, hence fulfilling the boundary condition (2.4) imposed by the uniform salinity profile. To trigger the instability, the initial temperature profile of Fig. 1 is perturbed by a random noise of small amplitude. Our series of simulations vary the Lewis number from 1 to 100, keeping the thermal diffusivity constant. The density ratio R_ρ varies from 1 to 406, tracking modifications in S_∞ . The parameters in Table 1 additionally prescribe the non-dimensional values: $Pr = 1$, $St = 2.4 \times 10^{-2}$ and $\gamma_1 = 2.8 \times 10^{-3}$, representative of polar ice–ocean conditions, though slightly idealised for numerical efficiency—in particular $Pr = O(10)$ in seawater.

3. Results

In all simulations, the fluid evolves through three main phases. This is illustrated in Fig. 2 (a,b), showing representative temperature and salinity snapshots. The system initially develops a Rayleigh–Taylor-like instability, which arises from the initially unstable buoyancy jump away from the interface (Drazin & Reid 2004; Boffetta & Mazzino 2017). This is followed by the interaction of the flow with the upper boundary and the onset of melting. Eventually, a mixing layer develops near the upper boundary and gradually deepens, with cold and fresh plumes extending downward into the domain. Note that contrary to previous studies with similar configurations (Guo & Yang 2025), we here focus on the transient dynamics before the turbulent layer reaches the bottom of the numerical domain and will not comment on the subsequent stationary (or quasi-stationary) states. Varying Le and R_ρ , the main difference

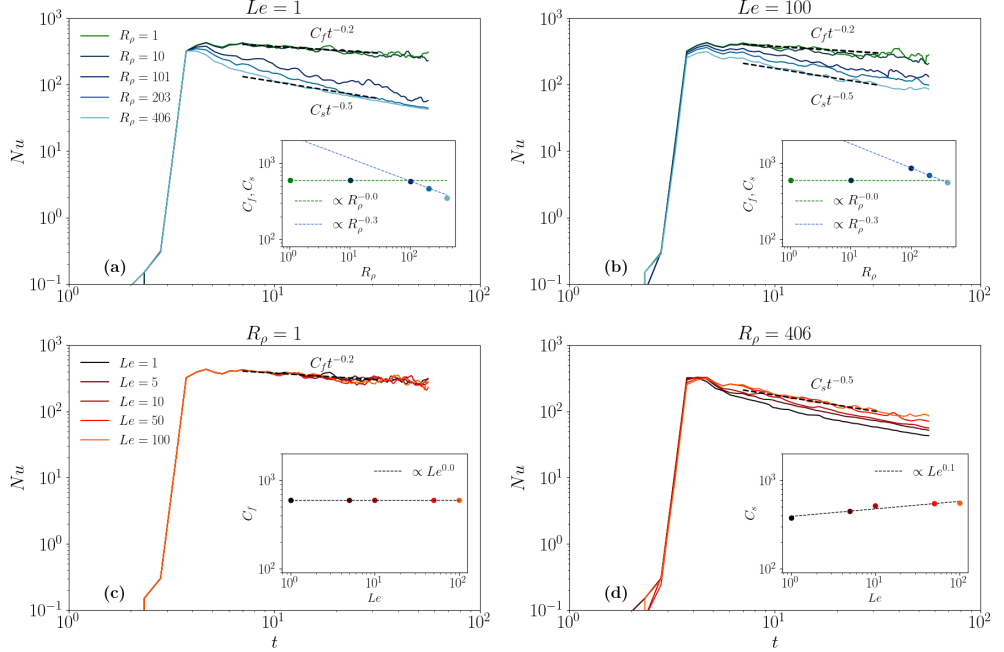


Figure 3: Time evolution of the Nusselt number Nu , varying R_ρ for fixed Le (top) and Le for fixed R_ρ (bottom). The insets display the prefactors C_s, C_f (see text).

is seen not in the bulk but at the melting interface. Increasing R_ρ , the top interfacial layer of fresh water gets thicker, as seen from the horizontally-averaged salinity profiles in Panels (c,d). No obvious difference is seen for the temperature, neither in the bulk nor at the interface. These observations suggests the following phenomenology: Salty environments favour strong stratification between the relatively fresh meltwater layer and the ambient ocean leading to a stable diffusive layer, while low density ratios favour mixing close to the upper interface.

3.1. Fluxes and temperature at the top interface

To quantify the melt-rate, we introduce the Nusselt number,

$$Nu = -\langle \partial_z \theta \rangle_{z=0}, \quad (3.1)$$

with $\langle \cdot \rangle$ denoting horizontal averaging. Analogous to Rayleigh–Bénard (RB) convection, the Nusselt number measures the thermal flux at the top boundary in units of the average temperature gradient $\Delta T/L_x$ —recall that $L_x = 1$ in our length units. It is directly proportional to the melt rate, $Nu \propto Le S_t \partial_z \theta|_{z=0}$. With the conventional minus sign in (3.1), the regime $Nu \geq 0$ reflects melting (this is the case under study) while $Nu < 0$ would indicate freezing.

Unlike RB convection, Nu decays over time. Its algebraic rate of decay exhibits two distinct asymptotic regimes, highlighting a strong dependence on the density ratio R_ρ and only a weak dependence on Le —see Fig. 3. In fresh environments, *i.e.*, for small values of $R_\rho \lesssim 10$, the Nusselt number decays only mildly as $Nu \sim C_f t^{-0.2}$, where both the exponent and the prefactor are insensitive to the Lewis number. In salty environments, *i.e.*, for large values of $R_\rho \gtrsim 10$, we observe a diffusive scaling $Nu \sim C_s t^{-0.5}$, with the prefactor following the apparent scaling law $C_s \sim Le^a R_\rho^b$. Our simulations indicate $b \simeq -0.3$ and $a \simeq 0.1$, meaning that the Lewis and density ratio have opposite effects, respectively enhancing and slowing melting in this apparent diffusive regime.

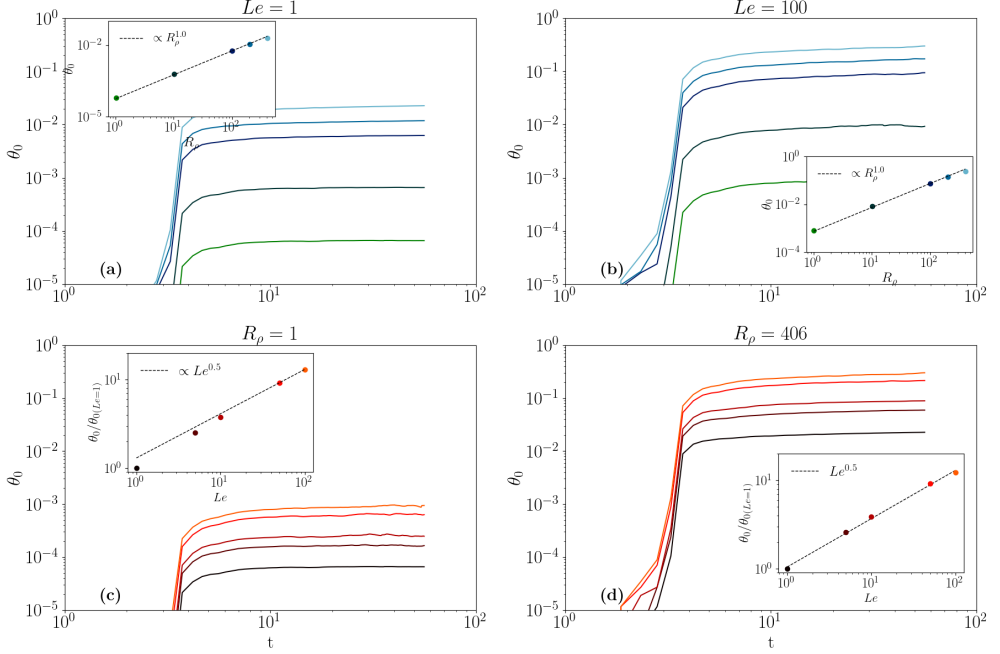


Figure 4: Time evolution of the interfacial temperature θ_0 , varying R_ρ at fixed Le (top) and Le at fixed R_ρ (bottom). The insets display the dependence on either R_ρ or Le averaging over times $t \gtrsim 10$.

The salinity at the boundary modifies the freezing temperature at the interface. Fig. 4 shows the evolution with time of the excess temperature (*i.e.*, above the freezing temperature based on the far-field salinity)

$$\theta_0 := 1 + \langle \theta \rangle_{x,z=0} = -\gamma_1 \sigma_0, \quad (3.2)$$

where $\sigma_0 = \langle \sigma \rangle_{x,z=0}$. The second equality indicates that θ_0 is proportional to the horizontally averaged fluctuation in salinity—see Eq. (2.4). Positive fluctuations $\theta_0 \geq 0$ are associated with fresh water at the interface, $\sigma_0 \leq 0$. Unlike the Nusselt number, no clear dichotomy emerges. In all the simulations, the top temperature quickly reaches a quasi-stationary value, which is characterised by the scaling behavior $\theta_0 \propto Le^{0.5} R_\rho$. This scaling is consistent with the intuitive idea that saltier ambient water favors a comparatively fresher interfacial boundary layer near the top interface.

3.2. Mixing dynamics

Our setup employs a regularization that offsets, by a depth δ , the initial temperature jump between the ice and the underlying bulk fluid. This triggers a classical Rayleigh-Taylor turbulent mixing layer. Without an upper boundary, the layer would grow quadratically $L(t) \sim t^2$ under a critical balance between buoyancy and nonlinear terms—this is the self-similar Bolgiano-Obukhov scenario (Chertkov 2003; Boffetta & Mazzino 2017). Interaction with the top interface, however, disrupts this classical regime. To characterise the mixing layer, we average over the horizontal direction to compute the profiles of temperature and salt, together with their associated vertical fluxes, *i.e.*,

$$\phi_\theta = \langle \theta u_z - Re^{-1} Pr^{-1} \partial_z \theta \rangle, \quad \text{and} \quad \phi_\sigma = \langle \sigma u_z - Re^{-1} (Le Pr)^{-1} \partial_z \sigma \rangle. \quad (3.3)$$

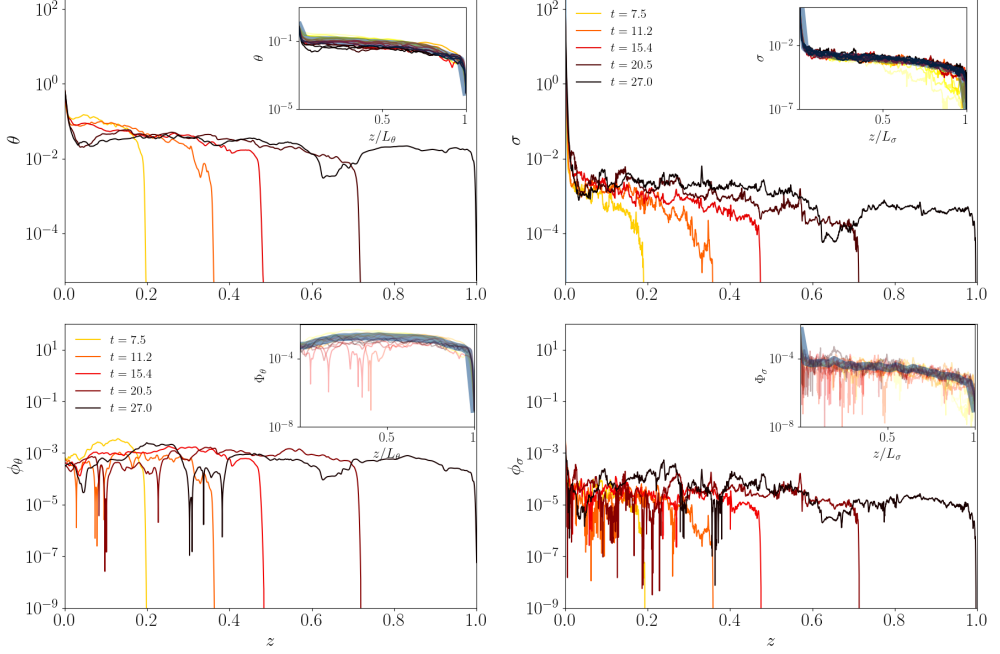


Figure 5: Vertical profiles (top) and fluxes (bottom) associated to heat (left panels) and salt (right panels) at successive times for the run at $Le = 100$ and $R_\rho = 406$. In insets, the profiles in terms of the rescaled coordinates z/L along with their mean (thick blue line).

Figure 5 uses the most salty environment $R_\rho = 406$ at $Le = 100$ to illustrate the typical behaviour. At a prescribed time, both profiles and fluxes fluctuate in z about a nearly constant value before dropping sharply. We use this drop to define the fronts $L_\theta(t)$ and $L_\sigma(t)$. Both fronts reach the bottom interface at $t \simeq 27$, and are synchronized with one another from $t \simeq 2$. They propagate at the common non-quadratic rate,

$$L_\theta \sim L_\sigma \sim C t^\beta, \quad C \approx 0.015, \quad \beta \simeq 1.33 \quad (3.4)$$

which seems largely independent of the density ratio R_ρ —see Fig. 6. We later refer to this common rate as $L(t)$. Combined together, Figures 5 & 6 and Eq. (3.4) suggest that the fronts evolve self-similarly, with mean profiles and fluxes given by

$$\langle \theta \rangle(z, t) \sim \Theta \left(\frac{z}{L(t)} \right) + \text{fluctuations}, \quad \phi_\theta(z, t) \sim \Phi_\theta \left(\frac{z}{L(t)} \right) + \text{fluctuations}, \quad (3.5)$$

and analogously for salinity. To extract the universal profiles Θ , Φ_θ , etc., we suppress the fluctuations in Eq. (3.5) by first rescaling $z \rightarrow z/L(t)$ and then temporally averaging. The resulting profiles are shown in the insets of Fig. 5.

Figure 7 compares the shapes of flux profiles Φ_θ and Φ_σ when varying R_ρ . The first observation is that the heat fluxes are largely independent of the density ratio. There is a slight enhancement of heat flux as R_ρ decreases below 10, marking a transition between salty and fresh environments. The transition in fact appears clearly when measuring the salt fluxes. These are constant within the mixing layer and peaked at the melting interface, indicating formation of a fresh meltwater layer that decouples the solid interface from the turbulent bulk. We measure the amplitude of the salt-layer induced decoupling by comparing the flux of fresh water at the interface, dominated by diffusion, with that at $z = L/2$ in the

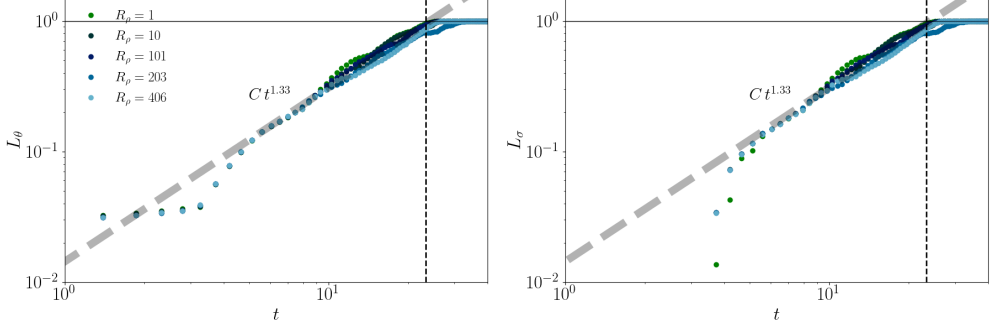


Figure 6: Time evolution of the temperature (left) and salinity (right) mixing lengths at $Le = 100$ for various density ratios. The vertical dashed line marks the time at which the fronts reach the bottom boundary.

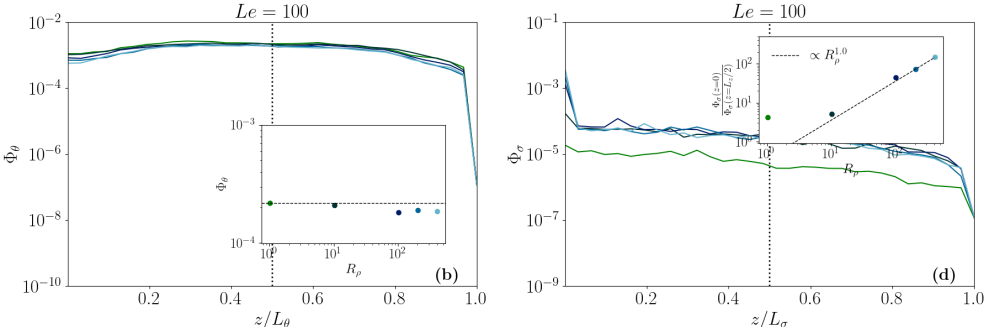


Figure 7: Mean vertical profiles of heat and salt fluxes for various density ratios at $Le = 100$. The insets in each panel display the values as the ice interface as functions of the density ratio, evaluated at the time indicated by the dot-dashed line.

midst of the turbulent layer—dominated by convection. The ratio between the diffusive and convective fluxes is constant in the fresh case, $R_\rho \lesssim 10$, and increases linearly with R_ρ in the salty case, $R_\rho \gtrsim 10$. This transition is compatible with that observed in Fig. 3 for the Nusselt number: the diffusive decay is associated to the formation of a diffusive layer near the interface. Note, however, that this layer does not impact the turbulent mixing within the bulk, and only regulates the amount of salt deficit injected into it.

3.3. Comments on mixing lengths

At high R_ρ , the physics involves an interplay between turbulent and diffusive flows, making the interpretation of mixing lengths strongly dependent on their definition. The mixing length $L(t)$ used in the previous section tracks the turbulent front, and is hence unaffected by the the fresh boundary layer. This length is measured by thresholding both temperature and salinity concentration at a very small value $\sim 10^{-12}$. It emphasises the role of thermally-induced convection and is largely independent of Le and double-diffusive effects within the bulk.

Among various options, the temperature and salinity mixing layers could be defined from different threshold values, as illustrated in Fig. 8. We observe that the temperature mixing layer exhibits the universal super-diffusive growth $Ct^{1.33}$ prescribed by Eq. (3.4) regardless of the selected threshold. In contrast, the salinity mixing layer exhibits a strong dependence on the chosen threshold. For small thresholds, the definition captures the turbulent front, and the growth remains as $Ct^{1.33}$. Increasing the threshold, the mixing length captures the

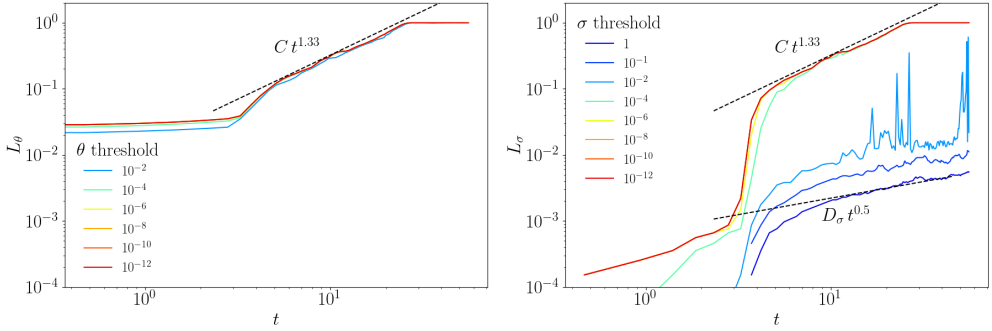


Figure 8: Temporal evolution of the mixing lengths for temperature (left) and salinity (right) using various thresholds for $Le = 100$ and $R_\rho = 406$.

near-interfacial dynamics, driven by the fresh, stably stratified meltwater layer. In this case, the salinity mixing length grows diffusively as $L_\sigma \sim D_\sigma t^{1/2}$, with a prefactor D_σ that depends on the threshold value.

These results highlight the sensitivity of mixing diagnostics to their precise definition. Here, different thresholds probe distinct physical processes, from turbulent transport in the bulk to diffusion-dominated dynamics near the interface. This sensitivity suggests potential caveats in more complex oceanographic settings, where mixed-layer depths are commonly defined using threshold-based criteria (de Boyer Montégut 2024; Allende *et al.* 2023).

4. Concluding remarks

We have examined the melt-driven convection beneath an ice–ocean interface. Consistent with previous studies (Xue *et al.* 2024), our setting exhibits a subdiffusive-dominated regime at small R_ρ and a diffusion-dominated regime at large R_ρ . However, we find that the diffusive dynamics remain confined only to a thin interfacial layer, with the bulk flow evolving through a (turbulent) convective thermal layer. Regardless of the near-interface regime, the front of this layer grows super-diffusively as $L \propto t^{1.33}$ for all R_ρ and Le . This scaling differs from the t^2 growth associated with Rayleigh–Taylor convection (Boffetta & Mazzino 2017), reflecting the presence of a rigid lid at the top boundary. The melting boundary condition controls the amount of salt in the bulk, with the fresh water input rate decreasing asymptotically as R_ρ^{-1} for large density ratios. While strongly idealised, our setting therefore exhibits a non-trivial interplay between a diffusive interfacial layer and a turbulent interior, emphasising the role of turbulence in regulating meltwater transport in high-salinity environments.

Open questions relate to the universality of this interplay. Beyond key physical parameters (dimensionality, initial stratifications, non-stationarity), the sharp interfacial gradient at the top interface makes the initial configuration effectively singular, with potential implications for its statistical predictability—see, *e.g.* (Biferale *et al.* 2018; Thalabard *et al.* 2020). To control the regularisation of the initial singularity, we chose to initiate melting through a thermal Rayleigh–Taylor instability slightly offset from the interface. This physical regularisation enables the boundary conditions to be explicitly enforced at early times, and triggers the convective turbulent layer. While no dependence on $\delta \rightarrow 0$, was found, it remains unclear whether such turbulent generation is universal across different regularisation schemes—in particular implementations relying on implicit regularisations only through numerical discretisation. This is a matter for future work.

REFERENCES

ALLENDE, S., FICHEFET, T., GOOSSE, H. & TREGUIER, A.-M. 2023 On the ability of oomip models to simulate the ocean mixed layer depth and its seasonal cycle in the arctic ocean. *Ocean Modelling* **184**, 102226.

ALLENDE, S., TREGUIER, A.-M., LIQUE, C., DE BOYER MONTÉGUT, C., MASSONNET, F., FICHEFET, T. & BARTHÉLEMY, A. 2024 Impact of ocean vertical-mixing parameterization on arctic sea ice and upper-ocean properties using the NEMO-SI3 model. *Geoscientific Model Development* **17** (20), 7445–7466.

BERHANU, M., PHILIPPI, J., COURRECH DU PONT, S. & DERR, J. 2021 Solutal convection instability caused by dissolution. *Physics of Fluids* **33** (7).

BIFERALE, L., BOFFETTA, G., MAILYBAEV, A. & SCAGLIARINI, A. 2018 Rayleigh-taylor turbulence with singular nonuniform initial conditions. *Physical Review Fluids* **3** (9), 092601.

BOFFETTA, G. & MAZZINO, A. 2017 Incompressible Rayleigh–Taylor turbulence. *Annual Review of Fluid Mechanics* **49** (1), 119–143.

DE BOYER MONTÉGUT, C. 2024 Mixed layer depth over the global ocean. *SEANOE [data set]* **10**, 98226.

CHERTKOV, M. 2003 Phenomenology of Rayleigh-Taylor turbulence. *Physical review letters* **91** (11), 115001.

COHEN, C., BERHANU, M., DERR, J. & COURRECH DU PONT, S. 2020 Buoyancy-driven dissolution of inclined blocks: Erosion rate and pattern formation. *Physical Review Fluids* **5** (5), 053802.

COUSTON, L.-A. 2024 Turbulent ice-ocean boundary layers in the well-mixed regime: insights from direct numerical simulations. *Journal of Physical Oceanography* .

DRAZIN, P. & REID, WILLIAM H. 2004 *Hydrodynamic stability*. Cambridge university press.

DU, Y., CALZAVARINI, E. & SUN, C. 2024 The physics of freezing and melting in the presence of flows. *Nature Reviews Physics* **6** (11), 676–690.

FAVIER, B., PURSEED, J. & DUCHEMIN, L. 2019 Rayleigh–Bénard convection with a melting boundary. *Journal of Fluid Mechanics* **858**, 437–473.

GASTINE, T. & FAVIER, B. 2025 Rotating convection with a melting boundary: An application to the icy moons. *Icarus* **429**, 116441.

GAYEN, B., GRIFFITHS, R. & KERR, R. 2016 Simulation of convection at a vertical ice face dissolving into saline water. *Journal of Fluid Mechanics* **798**, 284–298.

GUO, R. & YANG, Y. 2025 The effects of double diffusive convection on the basal melting of solid ice in seawater. *Journal of Fluid Mechanics* **1013**, A24.

HEWITT, I. 2020 Subglacial plumes. *Annual Review of Fluid Mechanics* **52** (1), 145–169.

HUPPERT, H. 1990 The fluid mechanics of solidification. *Journal of Fluid Mechanics* **212**, 209–240.

JENKINS, A. 1999 The impact of melting ice on ocean waters. *Journal of physical oceanography* **29** (9), 2370–2381.

KEITZL, T., MELLADO, J.-P. & NOTZ, D. 2016 Impact of thermally driven turbulence on the bottom melting of ice. *Journal of Physical Oceanography* **46** (4), 1171–1187.

MIDDLETON, L., VREUGDENHIL, C., HOLLAND, P. & TAYLOR, J. 2021 Numerical simulations of melt-driven double-diffusive fluxes in a turbulent boundary layer beneath an ice shelf. *Journal of Physical Oceanography* **51** (2), 403–418.

RAMADHAN, A., WAGNER, G., HILL, C., CAMPIN, J.-M., CHURAVY, V., BESARD, T., SOUZA, A., EDELMAN, A., FERRARI, R. & MARSHALL, J. 2020 Oceananigans. jl: Fast and friendly geophysical fluid dynamics on GPUs. *Journal of Open Source Software* **5** (53).

ROSEVEAR, M.G., GAYEN, B., VREUGDENHIL, C.A. & GALTON-FENZI, B.K. 2025 How does the ocean melt antarctic ice shelves? *Annual Review of Marine Science* **17**.

THALABARD, S., BEC, J. & MAILYBAEV, A. A. 2020 From the butterfly effect to spontaneous stochasticity in singular shear flows. *Communications Physics* **3** (1), 122.

VREUGDENHIL, C. & TAYLOR, J. 2019 Stratification effects in the turbulent boundary layer beneath a melting ice shelf: Insights from resolved large-eddy simulations. *Journal of Physical Oceanography* **49** (7), 1905–1925.

WETTLAUFER, J. 2001 The Stefan problem: Polar exploration and the mathematics of moving boundaries. *Die Zentralanstalt für Meteorologie und Geodynamik, 1851–2001, 150 Jahre Meteorologie und Geophysik in Österreich* pp. 420–435.

XUE, Z.-H., ZHANG, J. & NI, M.-J. 2024 Flow regimes in a melting system composed of binary fluid: transition from penetrative convection to diffusion. *Journal of Fluid Mechanics* **998**, A14.

YANG, R., XU, D., VERZICCO, R. & LOHSE, D. 2025 Asymmetric equilibrium states for melting and freezing in thermal convection. *Journal of Fluid Mechanics* **1017**, A12.